Physica 113B (1982) 284–298
North-Holland Publishing Company

ac AND dc CONDUCTION IN ELECTRO-ACOUSTICALLY ACTIVE CdS

W. WESTERA

Physics Laboratory, State University of Utrecht, Princetonplein 5, P.O. Box 80 000, 3508 TA Utrecht, The Netherlands

Received 1 December 1981

The ac impedance, in the frequency range 400 kHz to 100 MHz, and current saturation were investigated in electro-acoustically active semiconducting and photoconducting CdS single crystals. The measurements were carried out under pulsed bias conditions to avoid excessive Joule heating. The experimental results are discussed in terms of our previously published theory. The latter is based on a model according to which bunches of conduction electrons can be trapped and detrapped in potential troughs associated with acoustic waves which are amplified from the thermal background. The ac-impedance data show two low-frequency roll-offs obscured by potential trough transit-time resonances. At frequencies above 10 MHz an impedance plateau is observed. Theoretical results for the ac impedance could be fitted to the experimental results. From the observed resonance frequencies we were able to determine the potential trough transit time. The velocity of potential troughs was found to correspond to the group velocity of transverse amplified acoustic waves. No essential differences between semiconducting and photoconducting samples were observed. Furthermore it was found that the off-axis angle of maximum sound amplification is very sensitive to acoustic scattering losses at the sample boundaries. Experimental data at 77 K did not differ essentially from data at room temperature.

1. Introduction

Current saturation in piezoelectric semiconductors has been a subject of continuous interest, ever since Smith [1] in 1962 reported the first experimental data on CdS, CdSe and GaAs. The observed current saturation could be related to the amplification of acoustic waves originating from the thermal background, as was first reported by Hutson et al. [2] in 1961. In 1962 White [3] gave a linear continuum theory for the amplification of acoustic waves in piezoelectric semiconductors. Current saturation, however, is not described by this theory. Smith [1], following a suggestion of Rose, proposed that the current saturation was caused by trapping of free charge carriers in potential troughs associated with the amplified acoustic waves via the piezoelectric effect.

So far no systematic experimental data have been reported on the ac impedance of these devices under current saturation conditions. Some ac-impedance spectra were presented in 1978 by Gielen and Zijlstra [4]. However, because the electrical contacts on their CdS platelets covered only a small part of the end-surfaces, the electric current was mainly determined by the ohmic, unsaturated fringe area. As a consequence, the observed current saturation was very weak, and no associated ac-impedance effects were observed either.

In 1980 Westera, Zijlstra and van Dijk [5, 6] calculated the ac impedance of electro-acoustically active semiconductors. Their calculation was based on the trapping and detrapping of groups of free charge carriers in potential troughs which move with the velocity of sound. Experimental results, which showed a low-frequency roll-off related to the potential trough lifetime and resonances related to the trough transit time, were in good agreement with the theoretical predictions.

Additional measurements of current noise spectra [7], however, showed significantly smaller trough lifetimes than those obtained from ac-impedance data. To account for this discrepancy,

the impedance calculation was extended by introducing two types of potential troughs, one related to waves travelling in the direction of the drifting carriers (forwards) and the other to waves travelling in the opposite direction (backwards), each with a different relaxation time [8].

The aim of this paper is to compare systematically experimental data on current saturation and ac-impedance spectra for semiconducting and photoconducting CdS single crystals with the theory given in [8]. Furthermore we shall use the value of the trough transit time, which can be obtained from the resonances in the ac impedance, to distinguish between the amplification of transverse and longitudinal waves. So far there has been considerable controversy about which type of acoustic wave is amplified in some photoconducting CdS samples in which the electric field is parallel to the c-axis. From the observed relatively high threshold fields for the occurrence of ultrasonic amplification some authors [1, 4, 9] have concluded that longitudinal on-axis waves are amplified. Others [3, 10] believe that transverse off-axis waves are amplified and that the threshold field is raised by the existence of bound electron states in the forbidden energy gap.

The theoretical results of [8] are summarized in section 2, the experimental arrangement is described in section 3, and experimental results are presented and discussed in section 4.

2. Theory

On the assumption that the observed electro-acoustic effects can be described by the trapping of bunches of free charge carriers in potential troughs associated with the amplified acoustic waves, Westera [8] gave a linear classical continuum theory of the electro-acoustic effect, which took anisotropy and dispersion effects into account. In this section we shall summarize these theoretical results.

We consider an n-type homogeneous piezoelectric semiconducting single crystal, where the electric field is applied along a symmetry axis, the x_3-axis. In the case of CdS the x_3-axis coincides with the c-axis. The sample is supplied with ohmic contacts at $x_3 = 0$ (cathode) and $x_3 = L$ (anode), where L is the contact spacing. These contacts are spread uniformly over the end-surfaces. It is assumed that two types of potential troughs are present and that the kinetics of the two types of troughs are independent. One type of trough is associated with forward travelling (amplified) waves; the second type with backward travelling (attenuated) waves. Therefore the two types of troughs have opposite velocity components along the x_3-axis. In section 4 it will be shown that the trough velocity can be associated with the group velocity of the acoustic waves.

It is assumed that the first type of trough contains N_1 and the second type N_2 electrons per trough, with N_1 and N_2 independent of x_3. Furthermore it is assumed that the stationary state value of the total local electron density n in the conduction band is equal to the thermal equilibrium density of free charge carriers. This assumption implies that there is space-charge neutrality in the stationary state. Then, it follows that $\bar{n}_{s_1}$ and $\bar{n}_{s_2}$, and therefore $\bar{n}_d$ as well, are independent of x_3, where $\bar{n}_{s_1}$ and $\bar{n}_{s_2}$ are the average local densities of bunched electrons in the two types of troughs respectively, and $\bar{n}_d$ is the average free electron density. The average total density of electrons in the conduction band is given by

$$\bar{n} = \bar{n}_d + \bar{n}_{s_1} + \bar{n}_{s_2} . \tag{1}$$

The following sign convention is used: $V > 0$ while $E < 0$ and $I < 0$, where V is the applied voltage, E the electric field strength and I the electric current.

Under these conditions it is found that the equation for the current–voltage (IV) charac-

teristic reads [8]:

$$\bar{I} = -\left(\frac{qA\mu_{33}\bar{n}_d}{L}\right)\bar{V} - qAv_{g_3}(\bar{n}_{s_1} - \bar{n}_{s_2}), \quad (2)$$

where A is the contact area, $-q$ the electron charge, μ_{33} an element of the electron mobility tensor and v_{g_3} the component of the trough velocity along the x_3-axis. It should be noted that in general $\bar{n}_d$, $\bar{n}_{s_1}$, $\bar{n}_{s_2}$ and v_{g_3} depend on $\bar{V}$.

The threshold voltage V_c for amplification of acoustic waves is determined by the phase velocity of on-axis waves (wave vector direction along the c-axis). So we have

$$V_c = v_s(0)L/\mu_{33}, \quad (3)$$

where $v_s(0)$ denotes the phase velocity of on-axis waves.

When $\bar{V} < V_c$ we have $\bar{n}_d = \bar{n}$, and $\bar{n}_{s_1} = \bar{n}_{s_2} = 0$. So, eq. (2) reduces to Ohm's law

$$\bar{I} = -\bar{V}/R, \quad (4)$$

where

$$R = L/qA\mu_{33}\bar{n}. \quad (5)$$

The ac impedance was calculated by considering plane wave solutions with a wave vector in the direction of the unit vector $\boldsymbol{\kappa}$, and by assuming that the amplification of a wave is close to unity over one wavelength. If the crystal end-surfaces are free, the ac impedance Z is found to be given by

$$Z(\omega) = \{1 + \Psi(\omega)\} \times L\Big/A\left(q\mu_{33}\bar{n}_d + \frac{\alpha_1\tau_1}{1+i\omega\tau_1} + \frac{\alpha_2\tau_2}{1+i\omega\tau_2} + i\omega\varepsilon_{33}\right), \quad (6)$$

where ω is the angular frequency, and ε_{33} is an element of the permittivity tensor. τ_1 and τ_2 are the mean lifetimes of fluctuations in the trough densities n_{t_1} and n_{t_2}. If p_1 and b_1 are the creation and annihilation rate per unit volume of forward travelling troughs, respectively, τ_1 is given by

$$\tau_1 = -\left[\frac{\partial}{\partial n_{t_1}}(p_1 - b_1)\right]^{-1}_{\Delta n_{t_1}=0}. \quad (7)$$

Analogously τ_2 is given by

$$\tau_2 = -\left[\frac{\partial}{\partial n_{t_2}}(p_2 - b_2)\right]^{-1}_{\Delta n_{t_2}=0}. \quad (8)$$

In addition we have

$$\alpha_1 = qN_1(\bar{v}_{d_i} - v_{g_i})\kappa_i\left[\frac{\partial}{\partial E_j}(p_1 - b_1)\right]_{\Delta E_j=0}\kappa_j, \quad (9)$$

$$\alpha_2 = -qN_2(\bar{v}_{d_i} + v_{g_i})\kappa_i\left[\frac{\partial}{\partial E_j}(p_2 - b_2)\right]_{\Delta E_j=0}\kappa_j, \quad (10)$$

(summation over repeated indices; Einstein convention) where $\bar{v}_{d_i}$ is the ith component of the drift velocity given by

$$\bar{v}_{d_i} = -\mu_{ij}\bar{E}_j, \quad (11)$$

where μ_{ij} are elements of the electron mobility tensor. Obviously the quantities α_1 and α_2 are related to the field dependence of the trough creation and annihilation rates. Finally $\Psi(\omega)$ is a complicated complex function of ω, which describes the trough transit-time effects. It is found that $\Psi(\omega)$ contributes significantly only at frequencies given by

$$f = f_1 = \frac{(2l+1)}{2}\tau_t^{-1}; \qquad l = 0, 1, 2, 3, \ldots, \quad (12)$$

where $\tau_t = L/v_{g_3}$ is the trough transit time. Consequently $|Z(\omega)|$ will be found to show maxima at frequencies given by eq. (12).

Three limiting cases are of interest for our impedance measurements:

(i) When $\omega \to 0$ we obtain from eq. (6) for the

differential resistance R_d in the IV-characteristic:

$$R_d = Z(0) = \frac{L}{A(q\mu_{33}\bar{n}_d + \alpha_1\tau_1 + \alpha_2\tau_2)}; \quad (13)$$

(ii) When

$$\omega \gg \left| \left(q\mu_{33}\bar{n}_d + \frac{\alpha_1\tau_1}{1+i\omega\tau_1} + \frac{\alpha_2\tau_2}{1+i\omega\tau_2}\right) \Big/ \varepsilon_{33} \right| ,$$

we find

$$Z(\omega) \approx \frac{L}{i\omega A\varepsilon_{33}}, \quad (14)$$

which corresponds to the impedance of a device with capacity $C = \varepsilon_{33}A/L$;

(iii) At intermediate frequencies, where

$$\left| \frac{\alpha_1\tau_1}{1+i\omega\tau_1} + \frac{\alpha_2\tau_2}{1+i\omega\tau_2} + i\omega\varepsilon_{33} \right| \ll q\mu_{33}\bar{n}_d ,$$

we find an impedance plateau which is given by

$$Z(\omega) = \frac{L}{Aq\mu_{33}\bar{n}_d}. \quad (15)$$

3. Experimental arrangement

The devices used for our measurements were obtained from Eagle–Picher Industries, Inc. We used both semiconducting and photoconducting single crystals of hexagonal n-type CdS.

To make Brillouin scattering experiments possible at a later stage some crystal side faces were mechanically polished to a flatness of approximately $\frac{1}{4}\,\mu$m. As acoustic waves with frequencies around 1 GHz (wavelengths $\approx 2\,\mu$m) are expected to be amplified, it is obvious that the roughness of the crystal surfaces will influence the dynamics of the acoustic waves. In some cases the two contact faces were polished to a flatness of $\frac{1}{4}\,\mu$m as well. Unpolished surfaces can be expected to cause considerable acoustic scattering losses.

The samples were supplied with two In-evaporated ohmic contacts in such a way that the applied electric field was orientated along the c-axis (the longitudinal configuration). The In contacts covered the end-surfaces completely. Prior to the In-evaporation at 10^{-3} Pa, the contact surfaces were chemically cleaned and subjected to a 20 min low-energy (0.5 keV) Ar-ion bombardment. After the In-deposition the crystals were heated for about one hour at 150°C in a nitrogen atmosphere [4]. Thin copper wires were connected to the crystal contacts by tiny droplets of a two-component silver epoxy.

In table 1 the dimensions, dark conductivity at room temperature, and surface characteristics of the semiconducting (s) and photoconducting (p) CdS crystals are listed. The sample lengths were

Table 1
Dimensions, dark conductivity at room temperature and surface characteristics of the semiconducting (s) and photoconducting (p) CdS samples.

Sample	L (mm)	A (mm^2)	Dark conductivity (Ω^{-1} m^{-1})	Polished faces (mm^2)
s_1	1.76	1.24×0.55	6.6×10^{-1}	–
s_2	1.84	1.27×0.59	5.6×10^{-1}	–
s_3	1.63	1.78×0.48	9.5×10^{-1}	1.78×1.63-faces 1.78×0.48-faces
s_4	1.76	1.24×0.43	6.6×10^{-1}	1.76×1.24-faces
s_5	2.79	1.43×0.37	2.3	all faces
s_6	1.76	2.53×0.97	1.3	–
p_1	1.65	2.14×2.20	2.3×10^{-3}	–
p_2	1.14	1.81×0.76	5.5×10^{-1}	–

kept smaller than 3×10^{-3} m to suppress electro-acoustic domain formation, which would give rise to a highly non-uniform and non-stationary electric field distribution in the samples. It is known from potential probe experiments [1, 9] that in these short crystals the electric field is uniform even under current saturation conditions.

Except for the crystals s_3, s_4 and s_5, which were attached to a sample holder at a small area on one of the side faces to permit Brillouin scattering experiments, the samples were suspended freely in space by the copper wires. Obviously this experimental arrangement provides free end-surfaces, in accordance with the boundary conditions used in the calculations ([8], cf. section 2).

To control the conductivity of photoconducting crystals the samples were illuminated from the side with filtered light from a quartz–halogen lamp or with light from a krypton laser. The optical wavelengths were such that no band-to-band transitions were induced but the generation of carriers from local centres prevailed. Therefore the absorption coefficient of the light is small and the samples can be assumed to be homogeneously illuminated.

To avoid excessive Joule heating of the samples the high voltage was applied in pulses of 40 μs with a repetition rate of 4 Hz. These pulse lengths, which were much longer than the transit times of acoustic waves ($\approx 1\,\mu$s), allowed the samples to reach a stationary state within the duration of the pulse. Furthermore the samples were subjected to a room-temperature nitrogen or air flow.

The height of the voltage pulses was measured with a sample-and-hold circuit.

The experimental set-up for the ac-impedance measurements is shown in fig. 1. Voltage pulses from the pulse generator were fed into the low-pass filter to suppress the higher harmonics of the pulses. To suppress the high broad-band noise generated by the electro-acoustic effect (cf. [7]) we used an HP 8558 B spectrum analyzer

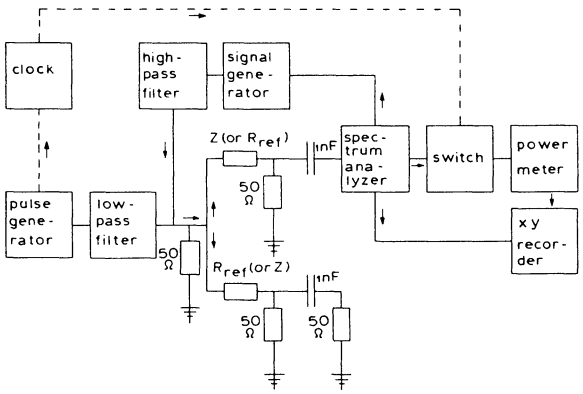

Fig. 1. Experimental set-up for measurements of the absolute value of the ac impedance $|Z|$ of the sample under pulsed bias conditions.

(input resistance 50 Ω) as a tunable band-pass filter. The high-pass filter protected the output stage of the signal generator against remaining transients of the voltage pulse. The IF-output (21.4 MHz) of the spectrum analyzer was fed into a switch (insulation > 110 dB) which only transmitted the signal between 5 and 35 μs after the onset of the bias pulse. The switch and the pulse generator were synchronised by the clock. The transmitted power was measured with an HP 8484 A power sensor combined with an HP 435 A power meter.

To determine the absolute value of the ac impedance $|Z|$ of the samples at a certain frequency we measured the power meter deflection P_1 (with the signal generator switched on) and the background power P_2 (signal generator switched off). The latter power was caused by the electro-acoustic current fluctuations and the noise of our measuring circuit. Thereupon we interchanged Z and the ohmic reference impedance R_{ref} (cf. fig. 1), and measured P_3 (signal generator switched on) and background power P_4 (signal generator switched off). It can be shown that

$$|Z + Z_s|^2 = \frac{P_3 - P_4}{P_1 - P_2} |R_{ref} + Z_s|^2 , \qquad (16)$$

where Z_s is the impedance in series with Z (or R_{ref}):

$$Z_s = R_0 \frac{1 + i\omega R_0 C_0}{1 + 2i\omega R_0 C_0}, \tag{17}$$

where $R_0 = 50\ \Omega$ and $C_0 = 1$ nF.

If $|Z|$ and R_{ref} (which was always chosen to be of the same order of magnitude as $|Z|$) are large compared to $|Z_s|$ eq. (16) reduces to

$$|Z|^2 \simeq \frac{P_3 - P_4}{P_1 - P_2} R_{ref}^2 . \tag{18}$$

The pulse length of 40 μs determines a fundamental low-frequency limit for the ac-impedance measurements. The low-frequency limit for our set-up turned out to be 400 kHz. The high-frequency limit for the ac-impedance measurements was 60 MHz to 100 MHz. This limit was set by the metal-film resistors which were used for reference, and by parasitic capacitances. The bandwidth of the spectrum analyzer was 300 kHz at frequencies below 10 MHz, and 1 MHz at frequencies above 10 MHz.

The signal generator was tuned automatically to the spectrum analyzer. Therefore, frequency-swept measurements were possible, using the frequency sweep of the spectrum analyzer. The power-meter deflection and the horizontal output of the spectrum analyzer (a measure for the operating frequency) were connected to an XY-recorder. The power-meter deflections P_1, P_2, P_3 and P_4 were recorded successively with frequency-sweep times of 500–1000 s.

The measuring procedure for the absolute value of the ac impedance under pulsed-bias conditions was checked by replacing the crystal by a known metal-film resistor. The results were in agreement with ac-impedance measurements obtained with other methods.

4. Experimental results and discussion

In this section we present and discuss the experimental results on semiconducting CdS (section 4.1) and photoconducting CdS (section 4.2). In section 4.3 ac-impedance data will be used to study the effects of scattering losses at the crystal side-faces. In section 4.4 data obtained at 77 K are shown.

4.1. Semiconducting CdS

In fig. 2 pulsed measured IV-characteristics are shown for the semiconducting samples s_1, s_3 and s_5. The characteristics are ohmic at low voltages, whereas strong current saturation is observed at high voltages. The dc low-voltage conductivity $\sigma = q\mu_{33}\bar{n}$ is determined with eq. (5) from the slope R^{-1} of the ohmic part of the IV-characteristic. From the literature [4, 6] it is known that the voltage defined by the onset of the electro-acoustic current fluctuations is a better indication for the threshold voltage V_c (cf. eq. (3)) than the knee voltage in the IV-charac-

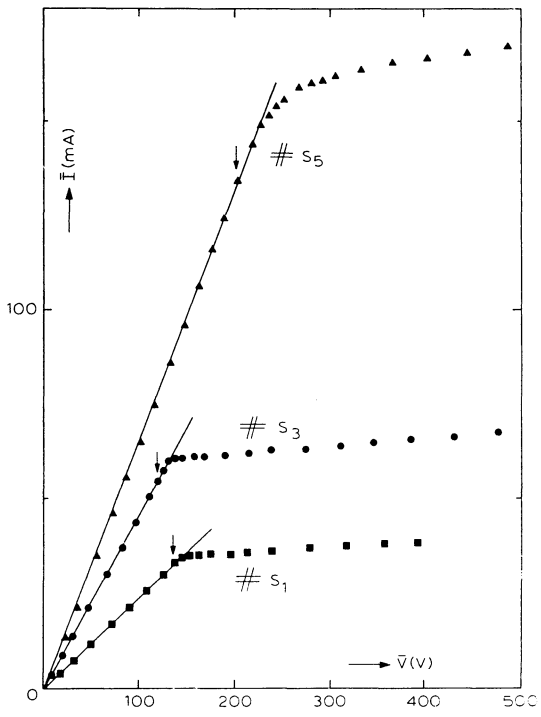

Fig. 2. Current–voltage characteristics for the semiconducting CdS samples s_1, s_3 and s_5. The solid lines represent Ohm's law. Arrows indicate the onset of electro-acoustic current fluctuations.

teristic. Therefore to determine V_c we measured the current noise power for each sample as a function of the applied voltage. For details about these current noise measurements we refer to [7].

The mobility values for CdS reported in the literature lie between $1.25 \times 10^{-2}\,m^2\,V^{-1}\,s^{-1}$ [11] and $3.88 \times 10^{-2}\,m^2\,V^{-1}\,s^{-1}$ [12] at room temperature. For this reason in most cases it is not possible to distinguish between transverse waves ($v_{s_0}(0) = 1.77 \times 10^3\,m\,s^{-1}$) and longitudinal waves ($v_{s_0}(0) = 4.41 \times 10^3\,m\,s^{-1}$) by using the experimental value of V_c and eq. (3).

In fig. 3 a typical result for the ac impedance as a function of frequency is shown for crystal s_6 at $(\bar{V} - V_c)/V_c = 0.19$. We observe an impedance plateau at frequencies above 10 MHz; this plateau corresponds to the plateau expected from eq. (15). The differential dc resistance R_d, which is indicated by an arrow on the vertical scale, differs markedly from the plateau value (cf. eq. (13)). Resonances, which appear to be the odd harmonics of $(4.33 \pm 0.05) \times 10^5$ Hz, are indicated by vertical arrows. From the observed resonances we find with eq. (12) a trough transit velocity of $v_{g_3} = (1.53 \pm 0.02) \times 10^3\,m\,s^{-1}$. This result enables us to distinguish between transverse and longitudinal acoustic waves.

The electro-mechanical coupling factor for

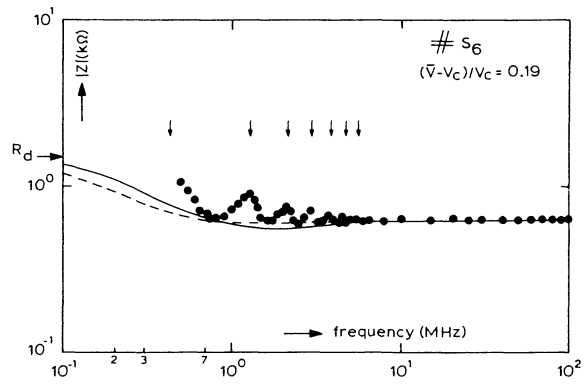

Fig. 3. The absolute value of the ac impedance of sample s_6 at $(\bar{V} - V_c)/V_c = 0.19$. The value of the differential resistance R_d is indicated on the vertical scale. The vertical arrows indicate odd harmonics of 4.33×10^5 Hz. The solid line and dashed line have been calculated with eq. (6), using the parameters listed in table A.1 (appendix).

longitudinal waves shows a maximum for waves travelling along the c-axis [13]. Therefore, if longitudinal acoustic waves are amplified in our samples these waves will be primarily on-axis waves. Then, the associated trough velocity, be it a phase or a group velocity, will be on-axis as well, with a magnitude close to $4.4 \times 10^3\,m\,s^{-1}$. It is concluded that the trough transit velocity v_{g_3} obtained from the resonances in fig. 3 cannot be explained by the amplification of longitudinal waves. From the literature [13] it is known that transverse off-axis waves may be amplified as well. The phase and group velocity of these waves have magnitudes around $2 \times 10^3\,m\,s^{-1}$. The value of $v_{g_3} = 1.53 \times 10^3\,m\,s^{-1}$ may thus be interpreted as the x_3-component of the phase or group velocity of transverse off-axis waves.

The off-axis angle, δ, of maximum amplification increases with increasing field strength until it saturates at 30°, because there is a maximum in the electro-mechanical coupling factor for transverse waves at $\delta = 30°$ [13]. Due to scattering losses at the crystal side-faces this saturation value will in practice be somewhat lower than 30° [14, 15]. Note that δ is the angle between the phase velocity and the c-axis [13–16].

If we were to interpret the observed trough transit velocity $v_{g_3} = 1.53 \times 10^3\,m\,s^{-1}$ as the x_3-component of the (unstiffened) phase velocity of transverse off-axis waves [5, 6], we would find an off-axis angle of $\delta = 43°$. We used the elastic constants given in [17] and [18] to calculate the phase velocity as a function of the off-axis angle δ. It is concluded that the potential troughs do not move with the phase velocity, since the value of $\delta = 43°$, exceeding the saturation value of 30°, is very unrealistic.

An alternative explanation is that the potential troughs move with the group velocity of transverse off-axis waves. Due to the elastic anisotropy in CdS the direction and magnitude of the group velocity may differ considerably from the direction and magnitude of the phase velocity. If we neglect the effects of electro-acoustic dispersion [8, 16], the direction and magnitude of

the group velocity corresponding to a certain off-axis wave can be calculated using the elastic constants. We found that for an off-axis angle of $\delta = 25°$ the magnitude of the corresponding group velocity is 2.06×10^3 m s^{-1} and the angle between the group velocity and the c-axis is 42°. Thus the x_3-component of this group velocity is 1.53×10^3 m s^{-1}. Since an off-axis angle of $\delta = 25°$ is quite acceptable we conclude that the potential troughs move with the group velocity of transverse off-axis waves.

The resonances that appear in fig. 3 are much wider than those predicted by eq. (6). As was pointed out in [5, 6], however, we have in practice an angular distribution of amplified off-axis, waves, which results in a distribution of transit velocities. This explains the smoothing out of the resonances as predicted by the theory, where only one type of off-axis angle was considered.

In view of the increasing current saturation with increasing applied voltage (cf. fig. 1) we can expect α_1 in eq. (9) to be negative and α_2 in eq. (10) to be positive. (Note that $E < 0$ when $V > 0$.) The solid line in fig. 3 was obtained with eq. (6) with $\Psi \equiv 0$ by setting $\tau_1 = 2.8 \times 10^{-7}$ s, $\tau_2 = 5.7 \times 10^{-8}$ s, $\alpha_1 = -3.4 \times 10^6 (\Omega\,\mathrm{m\,s})^{-1}$, $\alpha_2 = 5.5 \times 10^6 (\Omega\,\mathrm{m\,s})^{-1}$ and $q\mu_{33}\bar{n}_d = 1.14\,(\Omega\,\mathrm{m})^{-1}$. In this calculation the impedance-plateau value, the differential resistance R_d and the relaxation time τ_2, which was obtained from current noise data [7], were used as input constants. Since no broadened resonances are described by eq. (6) we used, at low frequencies, only the experimental data close to the local minima at frequencies that are in between the resonance frequencies. The values of τ_1 and α_1 (and therefore α_2) were adjusted by a least-squares fitting procedure. The thus obtained smooth solid curve in fig. 3 shows a minimum, which is caused by the two roll-offs: at low frequencies we observe a roll-off due to forward travelling troughs: with increasing frequency this roll-off is counteracted by a (negative) roll-off (or rather roll-on) due to backward travelling troughs. It should be noted that the errors in τ_1, α_1 and α_2 may be considerable due to the concealment of the low-frequency roll-offs by the transit time resonances. The numerical values of τ_1, α_1 and α_2 mentioned above, although obtained with a least-squares fitting procedure, suggest a higher accuracy than can be obtained with the available experimental data. To illustrate this we varied the parameters τ_1, α_1 and α_2 somewhat. The dashed line in fig. 3, which was calculated with eq. (6) using $\tau_1 = 5.0 \times 10^{-7}$ s, $\tau_2 = 5.7 \times 10^{-8}$ s, $\alpha_1 = -1.6 \times 10^6\,\Omega^{-1}\,\mathrm{m}^{-1}\,\mathrm{s}^{-1}$, $\alpha_2 = 2.0 \times 10^6\,\Omega^{-1}\,\mathrm{m}^{-1}\,\mathrm{s}^{-1}$ and $q\mu_{33}\bar{n}_d = 1.14\,\Omega^{-1}\,\mathrm{m}^{-1}$, also provides quite an acceptable fit to the measurements. Therefore, special care should be taken about drawing quantitative conclusions from the magnitudes of the various parameters. Nevertheless we can conclude that the relaxation time τ_2 of backward-travelling troughs is considerably smaller than the relaxation time τ_1 of forward-travelling troughs. This is what one would expect, since the strong attenuation of backward-travelling potential waves will cause a decrease of the potential trough lifetime.

In fig. 4 ac-impedance data obtained at different applied voltages are shown for crystal s_3. The solid lines represent the best fits calcu-

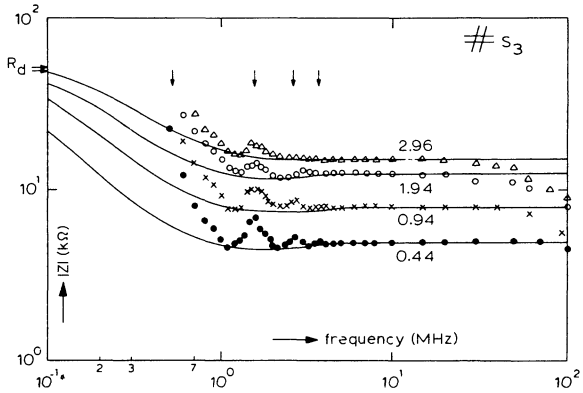

Fig. 4. The absolute value of the ac impedance $|Z|$ of sample s_3, at different applied voltages. The values of $(\bar{V} - V_c)/V_c$ are indicated. The vertical arrows represent odd harmonics of 5.15×10^5 Hz. The upper and lower values of the differential resistance R_d are denoted by arrows on the vertical scale. The solid lines have been calculated with the help of eq. (6). The parameters used are listed in table A.1 (appendix).

lated with the help of eq. (6), as discussed before. The values of α_1, α_2, τ_1, τ_2 and $q\mu_{33}\bar{n}_d$ are listed in table A.1 in the appendix. The differential resistance R_d turned out to be only weakly dependent on applied voltage (cf. fig. 2). The upper and lower values of R_d are indicated by arrows on the vertical scale. The observed resonances are interpreted as the odd harmonics of $(5.15 \pm 0.05) \times 10^5$ Hz, yielding a transit velocity of $(1.68 \pm 0.02) \times 10^3$ m s^{-1}. It should be noted that in this case we cannot unambiguously distinguish between the phase and the group velocity. If, again, we assume that potential troughs travel with the group velocity we find an off-axis angle of 13°. This value is considerably lower than the off-axis angle obtained for sample s_6. From earlier reports it is known [14, 15] that the off-axis angle of maximum amplification is strongly influenced by the dimensions of the sample, due to boundary scattering. From the dimensions in table 1 it seems plausible that in sample s_3 boundary scattering plays a more important role than in sample s_6.

Furthermore, it is observed that the resonances become less pronounced with increasing voltage. Note that the increase in the impedance-plateau value with increasing voltage indicates that the trapping of carriers in potential troughs increases with increasing voltage. The observed high-frequency roll-off may be due to an excess parasitic capacitance of approximately 1.4 pF parallel to Z_x (cf. fig. 1).

In fig. 5 we have plotted the value of the differential resistance R_d, obtained from the IV-characteristic, and the impedance-plateau value as a function of $\bar{V}/V_c$ for sample s_3.

When we use the measured IV-characteristic, and impedance-plateau values, we are able to calculate the electron densities $\bar{n}_d$, $\bar{n}_{s_1}$ and $\bar{n}_{s_2}$ as a function of the applied voltage. This was done with the help of eqs. (1), (2), (5) and (15). The mobility tensor element μ_{33} was determined from the onset voltage of the electro-acoustic current fluctuations (cf. eq. (3)). In fig. 6 the results of this calculation of the electron densities are given

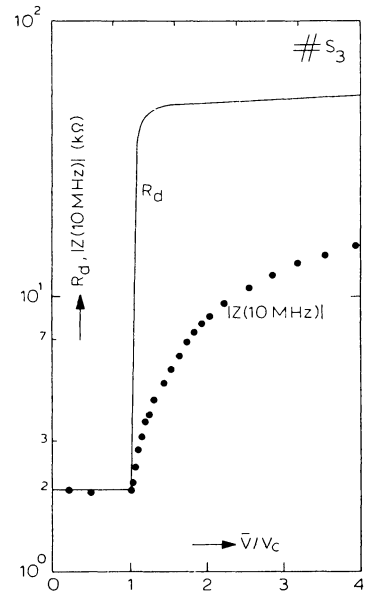

Fig. 5. The differential resistance (solid line) and the impedance-plateau value at 10 MHz (dots) as a function of $\bar{V}/V_c$ for sample s_3.

for sample s_3. For the value of v_{g_3} in eq. (2) we used 1.68×10^3 m s^{-1}, which was found from the resonance frequencies in fig. 4. We observe a decrease of the free electron density with increasing voltage, whereas the density of both

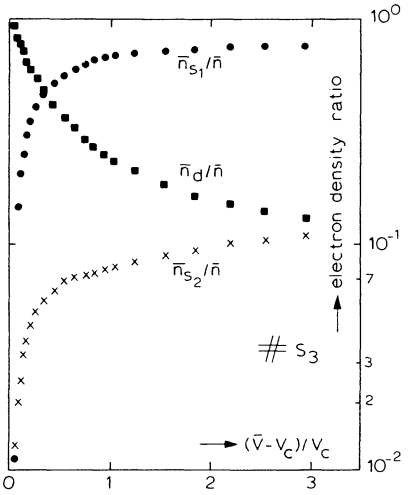

Fig. 6. The relative densities of free and trapped electrons as a function of $(\bar{V} - V_c)/V_c$ for sample s_3.

types of trapped electrons increases. Clearly the average trapping is dominated by the forward-travelling potential troughs. Similar results were obtained for the other samples.

4.2. Photoconducting CdS

In fig. 7 *IV*-characteristics are shown for samples p_1 and p_2 for different conductivities. The results are similar to those obtained for semiconducting CdS (cf. fig. 2).

Fig. 8 shows the results of the impedance measurements on sample p_2, at different applied voltages. The sample conductivity was $\sigma = 1.2\,(\Omega\,\mathrm{m})^{-1}$. The behaviour is found to be similar to that of the semiconducting samples: the plateau value increases steadily with increasing voltage, and resonances are observed, vanishing at higher voltages. At higher voltages the minimum in the smooth curves disappears as well. Note that fig. 8 shows a shift in the position of the resonances in the two lower curves. In the lower curve the resonances obviously coincide with the odd harmonics of 6.70×10^5 Hz, yielding a transit velocity of $1.53 \times 10^3\ \mathrm{m\,s^{-1}}$, whereas in the upper curve the resonance frequencies are given by the odd harmonics of 7.32×10^5 Hz, yielding $v_{g_3} = 1.67 \times 10^3\ \mathrm{m\,s^{-1}}$. At first sight this is contrary to

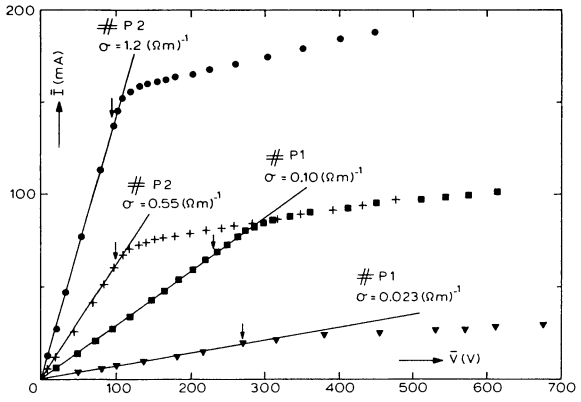

Fig. 7. Current–voltage characteristics for the photoconducting CdS samples p_1 and p_2 for different conductivities. The solid lines represent Ohm's law. Arrows indicate the onset of electro-acoustic current fluctuations.

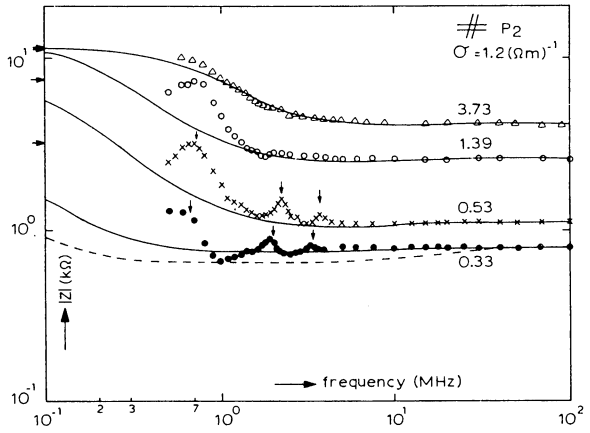

Fig. 8. The absolute value of the ac impedance of sample p_2 ($\sigma = 1.2\,(\Omega\,\mathrm{m})^{-1}$), at different applied voltages. The values of $(\bar{V} - V_c)/V_c$ are indicated. The magnitudes of the differential resistances R_d are indicated by arrows on the vertical scale. The vertical arrows represent the odd harmonics of 6.70×10^5 Hz and 7.32×10^5 Hz respectively. The solid lines and the dashed line have been calculated with the help of eq. (6). The parameters used are listed in table A.1 (appendix).

what one would expect, because, with increasing voltage, the off-axis angle of maximum sound amplification will increase until it reaches its saturation value. Therefore, with increasing voltage, the projection of the group velocity along the x_3-axis should become smaller [16]. However, a second, counteracting process may be of importance. Keller [16] showed, using White's linear theory, that the magnitude and direction of the group velocity are changed by electro-acoustic interaction. In fact, an increase in electro-acoustic interaction has been found to cause an increase in the x_3-component v_{g_3} of the group velocity. Thus we can conclude that v_{g_3} will be raised with increasing voltage, due to electro-acoustic dispersion. Although Keller used White's theory, which is certainly not applicable in our case, his estimate of electro-acoustic dispersion provides a qualitative explanation for the observed shift in the resonance frequencies. The explicit calculation of electro-acoustic dispersion effects, when starting from the potential trough model [8], is beyond the scope of this paper.

It should be noted that similar effects were

found for the semiconducting samples s_2, s_5 and s_6. Apparently, in the case of sample s_3 these two competing effects compensated each other.

The solid lines in fig. 8 are calculated with the help of eq. (6), as indicated before. The solid line at $(\bar{V}-V_c)/V_c = 0.33$ could not be fitted very well. The dashed line represents another possible solution. The values of the various parameters are listed in table A.1 (appendix).

In fig. 9 the results obtained from the *IV*-characteristic and the impedance-plateau values for $\bar{n}_d/\bar{n}$, $\bar{n}_{s_1}/\bar{n}$ and $\bar{n}_{s_2}/\bar{n}$ are shown as a function of $(\bar{V}-V_c)/V_c$ for sample p_1, for two different conductivities. Qualitatively the voltage behaviour of the electron densities is similar to that of semiconducting crystals (cf. fig. 6). The trapping is observed to decrease with decreasing conductivity, although $\bar{n}_{s_2}/\bar{n}$ increases somewhat. Since $\bar{n}_{s_2}/\bar{n}$ is very sensitive to a small change in the *IV*-characteristic data we can conclude that the spread in $\bar{n}_{s_2}/\bar{n}$ is caused by the inaccuracy of the measurements.

As already might be noticed from fig. 7 we found for sample p_1 that the threshold voltage for the electro-acoustic effect is much larger than the value we would expect for the amplification of transverse waves. To illustrate this fig. 10 shows the *IV*-characteristics of sample p_1 at $\sigma = 0.1\,(\Omega\,\mathrm{m})^{-1}$ and of sample s_3. From table 1 it is

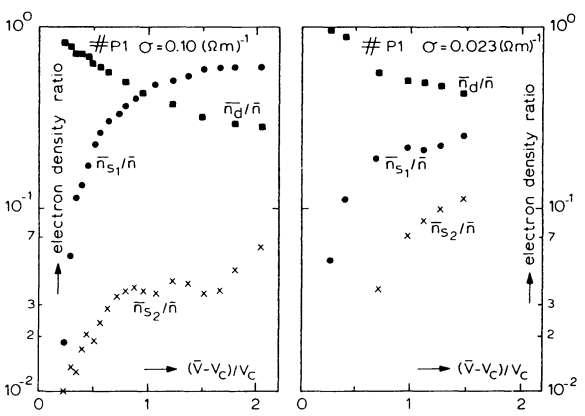

Fig. 9. The relative densities of free and trapped electrons as a function of $(\bar{V}-V_c)/V_c$ for sample p_1 for two different conductivities.

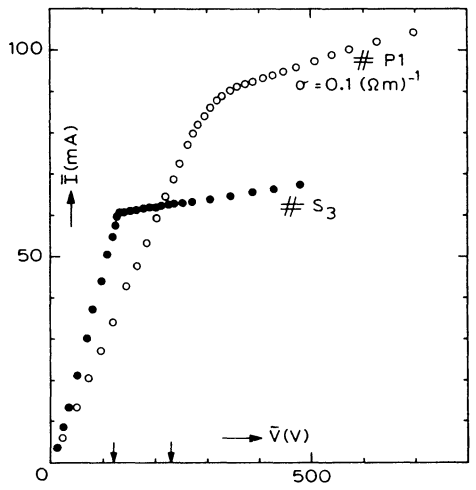

Fig. 10. The current–voltage characteristics of the photoconducting sample p_1 ($\sigma = 0.1\,(\Omega\,\mathrm{m})^{-1}$) and of the semiconducting sample s_1. The threshold voltages obtained from the onset of the electro-acoustic current fluctuations are indicated by arrows. The samples have equal contact spacings.

seen that these samples are almost equal in length.

In fig. 10 the threshold voltages obtained from the onset of the current fluctuations are indicated by arrows. In fact, it was found that $V_c = (119 \pm 5)$ V for sample s_3 and $V_c = (230 \pm 10)$ V for sample p_1. From these results one might easily be tempted to conclude that it is transverse waves which are amplified in sample s_3 ($v_{s_0}(0) = 1.77 \times 10^3\ \mathrm{m\,s^{-1}}$) and longitudinal waves in sample p_1 ($v_{s_0}(0) = 4.41 \times 10^3\ \mathrm{m\,s^{-1}}$) (cf. eq. (3)). Indeed several authors [1, 4, 9] have concluded from the high value they obtained for the threshold voltage in some photoconducting CdS crystals that longitudinal waves are amplified. However, no physical reason can be given as to why the transverse waves, which even have a higher electro-mechanical coupling factor than longitudinal waves, are not excited in these samples.

Therefore others [3, 10] suggested that the high value of the threshold field was due to the trapping of free charge carriers in bound electron states. Already in 1962 White [3] showed that these carrier trapping effects could be accounted

for by multiplying the carrier mobility by a factor f_0, where $0 \leqq f_0 \leqq 1$. Only a fraction f_0 of the electro-acoustically produced space charge is free and contributes to the conductivity. A fraction $(1 - f_0)$ of the space charge is produced by electrons trapped at states in the forbidden gap and is immobile. When μ_{33} is replaced by $f_0\mu_{33}$ in eq. (3), it is found that these trapping effects give rise to an increase in the threshold voltage.

This controversy can be removed if one measures the ac impedance, because the position of the resonances allows one to determine the trough transit velocity. Fig. 11 shows typical impedance measurements for both samples. Although the resonances for sample s_3 are somewhat more pronounced than those for sample p_1, it is clear that the resonances appear at the same frequencies. The arrows indicate the odd harmonics of 5.15×10^5 Hz, yielding a trough transit velocity of about 1.7×10^3 m s^{-1}. Thence, it is concluded that it is essentially transverse off-axis waves which are amplified in both semiconducting and photoconducting samples.

The experimental results, discussed above, strongly support the suggestion that the effect of carrier trapping in bound electron states plays an important role in some photoconducting CdS samples.

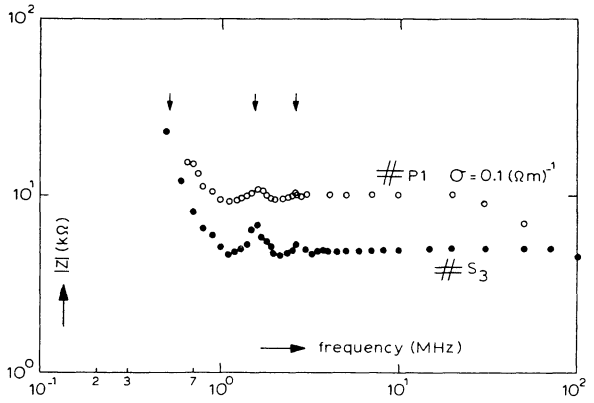

Fig. 11. Measurements of the absolute value of the ac impedance of sample p_1 (at $\sigma = 0.1\ (\Omega\ \mathrm{m})^{-1}$) and sample s_3. The vertical arrows represent the odd harmonics of 5.15×10^5 Hz.

4.3. Boundary scattering effects

In the calculation summarized in section 2 [8] the effect of the scattering of acoustic waves at the boundaries was not taken into account. In fact, in the calculation [8] the cross-sectional area A was assumed to be large with respect to L^2. In most experimental circumstances this assumption certainly does not hold, and considerable losses due to boundary scattering have been observed [14, 15].

The acoustic scattering losses at the side faces of our samples will affect acoustic waves with large off-axis angles most. This explains why in practice the observed off-axis angles of maximum sound amplification were smaller than 30°.

Since the off-axis angle of maximum sound amplification can be determined from the resonance frequencies in the impedance, our impedance measurements provide a convenient but indirect tool for studying these boundary scattering effects.

To investigate the effect of the boundary scattering we measured the ac impedance of sample s_1 at a certain electric field strength. As can be seen from table 1, all faces of sample s_1 are unpolished. Subsequently two side-faces of sample s_1 were polished to a flatness of $\frac{1}{4}\,\mu$m. This sample is renamed s_4, and is also listed in table 1. Since the wavelengths of the amplified acoustic waves are typically of the order of 2 μm (at 1 GHz) [3, 15], we expect a considerable reduction in the boundary scattering losses.

Again we measured the impedance at the same electric field strength as before.

In fig. 12 part of the impedance spectra is shown for both samples. The resonances observed for sample s_1 could be interpreted as the odd harmonics of 4.93×10^5 Hz (arrows), whereas for sample s_4 we found the odd harmonics of 4.60×10^5 Hz (arrows). If we neglect electro-acoustic dispersion effects these results yield $\delta \simeq 7°$ for sample s_1 and $\delta = 17°$ for sample s_4.

It is concluded that the off-axis angle of maximum sound amplification is strongly influenced

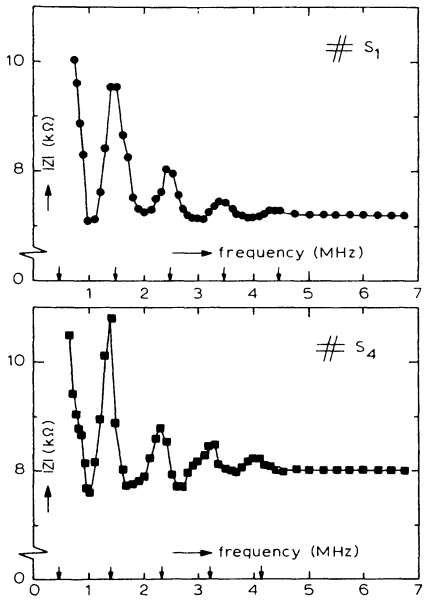

Fig. 12. The absolute value of the ac impedance for sample s_1 and sample s_4 at the same voltage. Resonance frequencies are indicated by arrows. The solid lines have been drawn to guide the eye.

by the sound wave scattering losses at the side-faces. No conclusions could be drawn from the experimental data about the influence of polished end-surfaces on the current saturation and the ac impedance.

4.4. Temperature effects

As the input of the sound amplification process is determined by the thermal acoustic energy distribution, we felt it was worthwhile to carry out measurements at different temperatures. Moore et al. [9, 19] found a strong increase in the ohmic slope in the *IV*-characteristic of semiconducting CdS when the temperature was changed from 293 K to 77 K. This was caused by an increase in the carrier mobility, whereas the carrier density remained almost constant. They found that the saturation current remained almost constant, as expected since it depends on the velocity of sound, which is nearly temperature independent. The results plotted as $\bar{I}$ vs. $\bar{V}/V_c$ were almost identical at different temperatures.

So far no reports have appeared in the literature about the temperature dependence of the ac impedance.

To carry out measurements at 77 K sample s_2 was simply immersed in liquid nitrogen.

Fig. 13 shows the *IV*-characteristics of sample s_2 at 293 K and 77 K. The arrows indicate the threshold voltages obtained from the onset of the electro-acoustic current fluctuations. If we assume the carrier concentration to be temperature independent [19] we find from the ohmic slopes that $\mu_{33}(77\text{ K})/\mu_{33}(293\text{ K}) \approx 7.4$. This is in agreement with the results obtained for the threshold voltages. From $V_c(293\text{ K}) = (142 \pm 5)$ V and $V_c(77\text{ K}) = (21 \pm 3)$ V it follows that (cf. eq. (3)) $\mu_{33}(77\text{ K})/\mu_{33}(293\text{ K}) = 6.8 \pm 1.0$. This ratio is not in agreement with literature values for the Hall mobility μ_H; these give values between 10 [20] and 15 [12] for $\mu_H(77\text{ K})/\mu_H(293\text{ K})$.

Moore et al. [19], who obtained from the threshold voltages a mobility ratio between 3 and 5.2, found from Hall measurements on the same samples $\mu_H(77\text{ K})/\mu_H(293\text{ K}) = 11$. They explained that this disagreement was due to the trapping of carriers in bound electron states in the forbidden gap. In fact, according to [3, 10] μ_{33} should be replaced by $f_0\mu_H$, where f_0 is the

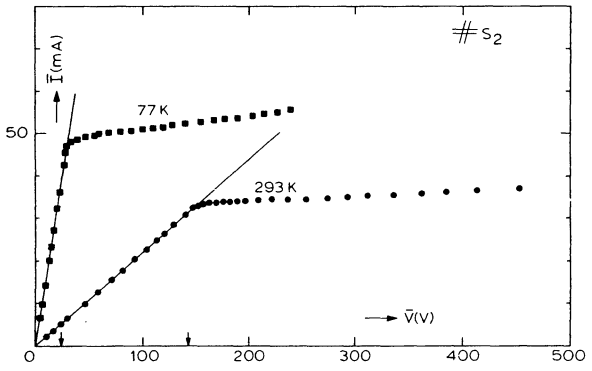

Fig. 13. Current–voltage relationships of sample s_2 at 293 K and 77 K. The arrows indicate the threshold voltages obtained from the onset of electro-acoustic current fluctuations. The solid lines represent Ohm's law.

fraction of the electro-acoustically produced space charge that is free (cf. section 4.2). Moore et al. [19] concluded that $f_0 = 1$ at room temperature and $f_0 = 0.3$–0.5 at 77 K.

It follows that the discrepancy between our data and the Hall mobility data in [20] can be removed by setting $f_0 = 1$ at room temperature and $f_0 \simeq 0.67$ at 77 K.

Furthermore the saturated current in fig. 13 is observed to be somewhat larger at 77 K than at 293 K. We found from the *IV*-characteristic and the impedance-plateau values that the trapping in potential troughs is less strong at 77 K. This was not reported by Moore et al. [9, 19]. However, it should be noted that the CdS samples used by Moore et al. had conductivities 20–200 times larger than sample s_2, and therefore showed stronger current saturation.

Another explanation for the observed reduction in the current saturation at 77 K may be a decrease in the sound amplification coefficient, which depends essentially on the carrier mobility. Furthermore the ultimate magnitude of the acoustic energy density may be reduced considerably by the reduced input of the sound amplification process at 77 K. Another possible explanation is a change in the acoustic reflection and transmission properties of the boundaries. Since the sample is immersed in liquid nitrogen a considerable amount of acoustic energy may be transferred into the ambient nitrogen.

In fig. 14 ac-impedance data at $\bar{V} = 194$ V are plotted for two temperatures. The solid lines have been calculated as indicated before, with the help of eq. (6) (cf. sections 4.1, 4.2). The behaviour of the ac impedance at 77 K is seen to be similar to that at room temperature. At 293 K the resonance frequencies, obviously the odd harmonics of 4.50×10^5 Hz, yield $v_{g_3} = 1.66 \times 10^3$ m s^{-1} and $\delta = 15°$. At 77 K the resonances can be associated with the odd harmonics of 4.67×10^5 Hz, yielding $v_{g_3} = 1.72 \times 10^3$ m s^{-1} and $\delta = 9°$. It should be noted that the effects of electro-acoustic dispersion are not taken into account in the determination of δ.

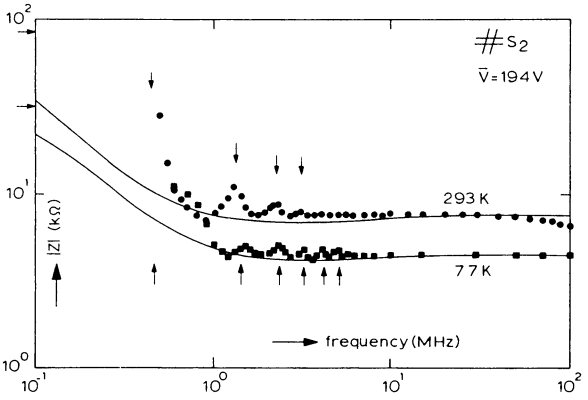

Fig. 14. The absolute value of the ac impedance of sample s_2 at 194 V for two temperatures. The values of the differential resistances are indicated by arrows on the vertical scale. The solid lines have been calculated with eq. (6). The parameters used are listed in table A.1 (appendix). The lower arrows indicate the odd harmonics of 4.67×10^5 Hz; the upper arrows represent the odd harmonics of 4.50×10^5 Hz.

We conclude that no fundamental changes occur in the current–voltage and impedance data when the temperature is changed from 293 K to 77 K.

Acknowledgements

The author is grateful to Professor C.Th.J. Alkemade and to Professor R.J.J. Zijlstra for their critical reading of the manuscript. This work was performed as part of the research programme of the "Stichting voor Fundamenteel Onderzoek der Materie" (FOM) with financial support from the "Nederlandse Organisatie voor Zuiver-Wetenschappelijk Onderzoek" (ZWO).

Appendix

In table A.1 we listed the parameter values used in the impedance calculations of figs. 3, 4, 8 and 14.

Table A.1

Sample	Fig.	$\frac{\bar{V}-V_c}{V_c}$	α_1 ($\Omega^{-1}\,m^{-1}\,s^{-1}$)	τ_1 (s)	α_2 ($\Omega^{-1}\,m^{-1}\,s^{-1}$)	τ_2 (s)	$q\mu_{33}\bar{n}_d$ ($\Omega^{-1}\,m^{-1}$)
s_6	3	0.19	-3.4×10^{6}	2.8×10^{-7}	5.5×10^{6}	5.7×10^{-8}	1.14
	3[a]	0.19	-1.6×10^{6}	5.0×10^{-7}	2.0×10^{6}	5.7×10^{-8}	1.14
s_3	4	0.44	-2.0×10^{6}	2.6×10^{-7}	1.9×10^{6}	8.4×10^{-8}	0.39
s_3	4	0.94	-1.2×10^{6}	2.4×10^{-7}	1.0×10^{6}	8.0×10^{-8}	0.24
s_3	4	1.94	-6.5×10^{5}	2.5×10^{-7}	5.7×10^{5}	7.6×10^{-8}	0.15
s_3	4	2.96	-4.7×10^{5}	2.2×10^{-7}	2.4×10^{5}	5.5×10^{-8}	0.13
p_2	8	0.33	-1.1×10^{6}	8.0×10^{-7}	5.0×10^{6}	1.1×10^{-8}	1.06
p_2	8[a]	0.33	-6.5×10^{5}	1.6×10^{-6}	2.2×10^{7}	1.1×10^{-8}	1.06
p_2	8	0.53	-3.4×10^{6}	2.0×10^{-7}	4.2×10^{6}	1.1×10^{-8}	0.75
p_2	8	1.39	-1.5×10^{6}	1.8×10^{-7}	1.7×10^{6}	1.1×10^{-8}	0.32
p_2	8	3.73	-1.8×10^{6}	7.8×10^{-8}	1.3×10^{6}	1.1×10^{-8}	0.20
s_2	14	0.36	-1.1×10^{6}	3.1×10^{-7}	2.4×10^{6}	1.6×10^{-8}	0.33
s_2	14[b]	8.1	-2.4×10^{6}	2.2×10^{-7}	3.5×10^{6}	2.0×10^{-8}	0.55

[a] Dashed line. [b] 77 K.

References

[1] R.W. Smith, Phys. Rev. Lett. 9 (1962) 87.
[2] A.R. Hutson, J.H. McFee and D.L. White, Phys. Rev. Lett. 7 (1961) 237.
[3] D.L. White, J. Appl. Phys. 33 (1962) 2547.
[4] P.A. Gielen and R.J.J. Zijlstra, Physica 95B (1978) 347.
[5] W. Westera, R.J.J. Zijlstra and M.A. van Dijk, Phys. Lett. 78A (1980) 371.
[6] W. Westera and R.J.J. Zijlstra, Physica 106B (1981) 33.
[7] W. Westera, Physica B, to be published.
[8] W. Westera, Physica 113B (1982) 149.
[9] A.R. Moore, J. Appl. Phys. 38 (1967) 2327.
[10] I. Uchida, T. Ishiguro, Y. Sasaki and T. Suzuki, J. Phys. Soc. Japan 19 (1964) 674.
[11] B. Pödör, J. Balázs and M. Hársy, Phys. Stat. Sol. (a) 8 (1971) 613.
[12] J.D. Zook and R.N. Dexter, Phys. Rev. 129 (1963) 1980.
[13] A.R. Moore, R.W. Smith and P. Worcester, IBM J. Res. Developm. 13 (1969) 503.
[14] O. Keller, Phys. Rev. B10 (1974) 1585.
[15] M. Yamada, C. Hamaguchi, K. Matsumoto and J. Nakai, Phys. Rev. B7 (1973) 2682.
[16] O. Keller, Phys. Sol. 16 (1973) 87.
[17] D. Berlincourt, H. Jaffe and L.R. Shiozawa, Phys. Rev. 129 (1963) 1009.
[18] I.B. Kobiakov, Sol. State Commun. 35 (1980) 305.
[19] A.R. Moore and R.W. Smith, Phys. Rev. A138 (1965) 1250.
[20] B. Pödör, Act. Phys. Ac. Sc. Hung. 36 (1974) 431.